IEEE Access
Multidisciplinary ⋮ Rapid Review ⋮ Open Access Journal

Received October 24, 2020, accepted December 2, 2020, date of publication December 7, 2020,
date of current version December 17, 2020.

Digital Object Identifier 10.1109/ACCESS.2020.3042854

Design of Eccentric Mass-Type Vibration-Damping Electric Actuator Control System for Non-Fixed-Wing Aircraft

ZHENYANG HAO, (Member, IEEE), TAO WANG, XIN CAO, (Member, IEEE), AND QIYAO ZHANG, (Student Member, IEEE)

Department of Electrical Engineering, Nanjing University of Aeronautics and Astronautics, Nanjing 210016, China

Corresponding author: Zhenyang Hao (zhenyang_hao@nuaa.edu.cn)

ABSTRACT The main spiral blade of non-fixed wing aircraft will produce periodic vibration force when rotating, which will not only reduce the service life of airborne equipment, but also greatly affect the working state of pilots. Due to the narrow damping band of passive damping device, it is difficult to meet the vibration reduction requirements of modern aircraft. Therefore, this article proposes an eccentric mass block type electrical control system based on active vibration control Force actuator system and a prototype is developed. In this article, the output force model of eccentric wheel type anti vibration actuator, the periodic fluctuating load model of motor side, the linearization model of gear clearance and the dynamic model of the whole electric actuator are established. Secondly, according to the system stability control requirements, the controller parameters of the electric actuator are designed. The maximum value of the gear clearance dimension is introduced into the control system to correct the controller parameters, and provide theoretical design basis for the actuator gear clearance size. Finally, the sensitivity function from the disturbance side to the control error side is calculated. The effectiveness of the parameters and the robustness of the control system are verified by the sensitivity H_∞ control theory. The results show that the prototype has good dynamic and steady-state performance and meets the vibration control requirements of the main spiral blade of the non-fixed wing aircraft.

INDEX TERMS Active vibration damping control, gear clearance, controller parameters, sensitivity H_∞ control, robustness.

I. INTRODUCTION

In the process of ground operation and air flight of non-fixed wing aircraft, under the joint action of airflow, rotor, tail slurry and other high-speed optional components, the airframe often produces serious vibration problems, and even leads to catastrophic aircraft damage and human death. Studies have shown that 40% of helicopter accidents are related to vibration. Therefore, the noise and vibration levels of fixed wing aircraft used by general have been included in the national military standard assessment range [1], [2]. At the same time, in order to improve the vibration environment of airborne equipment, improve its safety and reliability, and improve the working state of pilots, vibration reduction has become a research hotspot of major non fixed wing aircraft manufacturers and research institutions in the world [3], [4].

At present, there are mainly two kinds of damping technology: passive damping technology and active damping technology. Passive vibration reduction mainly uses vibration absorbers to absorb the vibration force of helicopters or use vibration isolators to suppress the transmission of vibration power, such as dynamic vibration absorbers, dynamic anti resonance isolators and other vibration absorption or vibration isolation devices [5]. Because of its simple structure, convenient operation, low price and other advantages, it has been widely used in the vibration reduction system of flyers. However, with the increasing flight height and speed of the aircraft, the flight environment is more complex. At the same time, with the further improvement of the aircraft transmission system and airborne equipment system integration,

The associate editor coordinating the review of this manuscript and approving it for publication was Juntao Fei.

the traditional passive vibration elimination method cannot meet the needs of aviation development due to the narrow working frequency band and low efficiency, so the active vibration elimination technology emerges as the times require.

For active vibration reduction, there are two main methods at present. One is the closed-loop control through the vibration signal collected by the vibration sensor, and the purpose of vibration control is achieved by modifying the parameters of the controlled object, which is mainly represented by the classical high-order harmonic control [6]. The other way is to control the actuator to generate the corresponding action force according to the vibration signal collected by the vibration sensor, so as to change the structure of the forced object or directly offset the vibration force to achieve the purpose of active vibration reduction. The vibration damping electric actuator is a typical active damping device, which can reduce vibration by ''vibration counteracting vibration'' [7]. The actuator is driven by two motors to drive a group of eccentric wheel loads to do high-speed circular motion in the vertical plane, thus generating sinusoidal centrifugal force, which is the driving force for system vibration reduction. The system controls the frequency, phase and amplitude of centrifugal force by adjusting the speed, position and position difference of two pairs of eccentric wheels, so as to deal with different vibration forces.

In reference [8], the X2 high-speed verification machine adopts active structural response control technology to solve the strong vibration problem at large forward flight speed [8]. An active shock absorber with adjustable time delay was designed in reference [9]. The vibration reduction effect of the shock absorber was improved by reasonable feedback gain and delay processing [9]. In reference [10], a six degree of freedom active vibration isolation platform (AVIP) is proposed by using modular design method, and the dynamic characteristics of AVIP and known AVIM are analyzed. It can isolate vibration with multiple degrees of freedom, and has large bearing capacity, wide frequency band and high vibration isolation accuracy [10]. The domestic research on active vibration control technology started late, mainly relying on the promotion of universities and research institutes. Reference [11] pointed out that researchers from Harbin Engineering University used LMS adaptive algorithm for frequency modulation control of ship vibration eliminator and self- optimization algorithm for phase modulation control, which fully verified the performance of vibration absorber and control system [11]. In reference [12], based on the establishment of the dynamic model of the vibration reduction comprehensive design system by using the finite element method, the vibration reduction characteristics of the main transmission channel isolation system (SARIB), vibration source control system (hub absorber) and fuselage vibration control system (actuator) were studied, and the comprehensive vibration reduction effect was analyzed [12]. Reference [13] introduces the main research work and achievements of active vibration isolation, active and semi-active vibration absorption of ship power plant and active vibration elimination technology of ship structure in Harbin Engineering University, which promotes the practical application of active vibration elimination technology in ships [13].

However, due to the fact that the vibration reduction frequency band of the non-fixed wing aircraft is much wider than that of the ship shock absorber, the control accuracy is required to be higher, and at the same time, there is a nonlinear problem of gear clearance in gear transmission system [14]. The existence of gear clearance not only increases the difficulty of motor control, but also greatly reduces the output performance of the system. In addition, the periodic sinusoidal load disturbance exerted by the eccentric mass on the motor side will cause torque ripple in the power actuator system, which reduces the stability margin of the power actuator control system, thus increasing the difficulty in the design of the system controller [15]. Based on this, this article first deduces and establishes the sub component model of the actuator system, including the output force model of the eccentric mass block type vibration elimination electric actuator, the periodic pulsating load model of the motor side, the linearization model of the gear clearance and the dynamic model of the whole electric actuator. Secondly, according to the working mechanism of the power actuator output force, the control strategy and control block diagram of the power actuator control system are proposed. Combined with the three-loop output force servo control strategy, the parameters of current loop, speed loop and position loop controller are designed for tuning calculation, which improves the dynamic and steady-state performance of the control system. At the same time, considering the influence of gear clearance nonlinearity on the control system in actual working conditions, the maximum value of the gear clearance size between the driving and driven wheels of the actuator is introduced into the parameter design of the closed-loop controller, and the parameters of the position loop regulator are corrected by the iterative calculation method, which provides the mechanical design basis for the size of the gear clearance, so that the control system has strong adaptive ability and can meet the requirements of the control system stability requirements under different gear clearance dimensions [16], [17]. Finally, the sensitivity function from the disturbance side to the control error side is calculated, and the effectiveness of the parameter design and the robustness of the control system are verified by using the sensitivity H_∞ control theory [18], [19].

At the same time, this article develops an engineering prototype of the eccentric wheel type vibration damping electric actuator, and completes the steady-state and dynamic performance verification experiments of force amplitude, frequency and phase, which further verifies the feasibility and correctness of the control strategy and controller parameter design, and provides certain technical support for its application in non-fixed wing aircraft.

II. MODEL DERIVATION AND ESTABLISHMENT OF ELECTRIC ACTUATOR SYSTEM WITH ECCENTRIC MASS

A. MODELING OF ACTUATOR OUTPUT FORCE

The structure of the electric actuator with eccentric mass is shown in Fig.1(a), which is composed of two pairs of symmetrical eccentric mass block type electric actuator. The electric actuating unit on each side is shown in Fig.1(b). The motor shaft of the outer rotor is tightly assembled with the driving wheel and drives the driving wheel. The driving wheel drives the eccentric mass block on the left driven wheel to rotate through the gear. At the same time, the driving wheel drives the eccentric mass on the right driven wheel through the idler gear. The effect of the idler makes the mass on both sides form relative motion. The rotation speed is the same but the direction is opposite so that the output of the centrifugal force generated by the rotation of the two masses is zero in the horizontal direction and changes sinusoidal periodically in the vertical direction. Similarly, a pair of eccentric masses on the other side also produce sinusoidal output force with the same amplitude and frequency. Therefore, the magnitude of the active output force can be controlled by controlling the phase difference of the two vertical forces. The working mechanism of the actuator is theoretically deduced below [20].

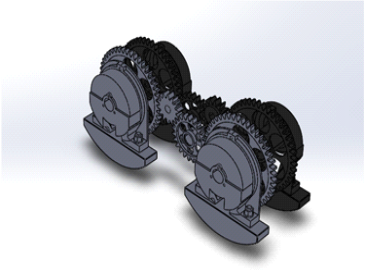

(a) 3D illustration of eccentric mass electric actuator.

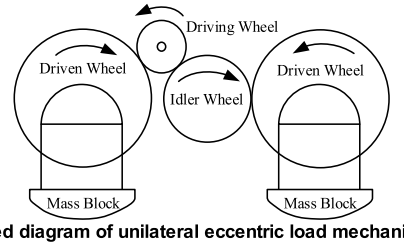

(b)Simplified diagram of unilateral eccentric load mechanical transmission structure.

FIGURE 1. Mechanical transmission structure diagram of eccentric load.

The force diagram of a pair of eccentric mass blocks is shown in Fig. 2 below. At the origin of X-Y axis coordinate system with the center symmetry point of the actuator as the output force, the mass block is regarded as the mass point.

The resultant force of the unilateral mass group output is as follows:

$$F_1 = 2m\omega_1^2 r\sin(\omega_1 t + \phi_1) \tag{1}$$

Similarly, the resultant force on the other side is:

$$F_2 = 2m\omega_2^2 r\sin(\omega_2 t + \phi_2) \tag{2}$$

Among them, m is the weight of a single mass block; ω is the angular frequency of the mass block rotation; ϕ_1 is the initial phase of the mass block; r is the radius of the mass block rotation.

In the end, the combined force output formula of the actuator is:

$$\begin{aligned} F_{out}(t) &= A_1\sin(\varphi_1) + A_2\sin(\varphi_2) \\ &= |F_{out}(t)|\sin(\measuredangle F_{out}(t)) \end{aligned} \tag{3}$$

Among them:

$$|F_{out}(t)| = \sqrt{A_1^2 + A_2^2 - 2A_1A_2\cos(\varphi_1 + \varphi_2)} \tag{4}$$

$$F_{out}(t) = \frac{\varphi_1 - \varphi_2}{2} + \tan^{-1}\left(\frac{A_1 + A_2}{A_1 - A_2}\tan\left(\frac{\varphi_1 + \varphi_2}{2}\right)\right) \tag{5}$$

$$\begin{aligned} A_1 &= 2m\omega_1^2 r \quad A_2 = 2m\omega_2^2 r \\ \varphi_1 &= \omega_1 t + \phi_1 \quad \varphi_2 = \omega_2 t + \phi_2 \end{aligned} \tag{6}$$

Especially, when $\omega_1 = \omega_2$, it has:

$$F_{out}(t) = 4m\omega^2 r\cdot\cos\left(\frac{\Delta\theta}{2}\right)\cdot\cos(\omega t + \phi) \tag{7}$$

Among them: $\Delta\theta_1 = \varphi_1 - \varphi_2$, $\phi = (\phi_1 + \phi_2)/2$.

In order to control the output force amplitude, as shown in Fig.3, the phase difference of the eccentric wheels on both sides should be closed-loop controlled.

$$\begin{aligned} \Delta\theta = \varphi_1 - \varphi_2 &= \int(\omega_1 + \Delta\omega_1)dt \\ &\quad - \int(\omega_2 + \Delta\omega_2)dt + \phi_1 - \phi_2 \\ &= \int(\omega_1 - \omega_2 + \Delta\omega_1 - \Delta\omega_2)dt + \phi_1 - \phi_2 \end{aligned} \tag{8}$$

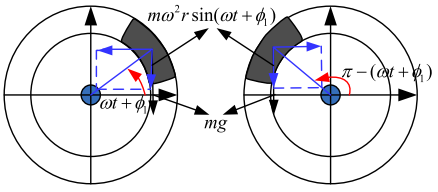

FIGURE 2. Force sketch of eccentric mass block group.

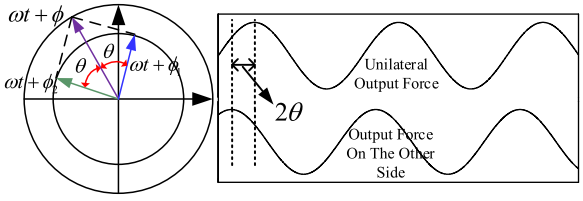

FIGURE 3. Schematic diagram of the output force of two pairs of eccentric masses.

Equation (8) is expressed in the discrete domain as:

$$\begin{aligned}\Delta\theta(n) &= \varphi_1(n) - \varphi_2(n) \\ &= \lim_{m\to\infty}\sum_{n=1}^{m}[\omega_1(n) - \omega_2(n) + \Delta\omega_1(n) - \Delta\omega_2(n)] \\ &\quad + \phi_1 - \phi_2 \\ &= \lim_{m\to\infty}\sum_{n=1}^{m}\Delta\omega(n) + \phi_1 - \phi_2 \end{aligned} \tag{9}$$

The necessary condition for convergence from infinite series is:

$$\lim_{n\to\infty}\Delta\omega(n) = 0 \tag{10}$$

According to equation (10), the premise of convergence of output force amplitude is that the rotation frequency difference of the eccentric wheels on both sides is zero, that is, the rotation speed is synchronous. At the same time, the smaller the fluctuation value of frequency difference near zero, the weaker the beat frequency phenomenon of output force. As shown in Fig. 4, the output force wave-forms with different rotation frequencies of the eccentric wheels on both sides of the actuator are represented by blue lines and the output force wave-forms with the same rotation frequency are represented by red lines. It can be seen that the rotation frequencies of the eccentric wheels on both sides of the actuator are inconsistent. The output force amplitude contour presents a periodic 'beat frequency phenomenon'.

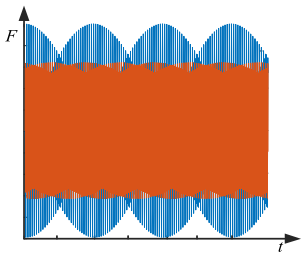

FIGURE 4. Beat waveform of output force.

B. LINEAR MODELING OF GEAR CLEARANCE IN TRANSMISSION MECHANISM

For the eccentric mass block type electric actuator system driven by motor, the clearance between the gears is designed to be more than 0.05mm in the actual project in order to improve the vibration mode at the rated frequency and increase the service life of the gear. So the nonlinearity caused by the gear clearance is one of the important factors in the system stability design. The hysteresis model, dead zone model and "vibro impact" model are most widely used for tooth clearance models. Among them, the hysteresis model reflects the displacement relationship of the master-slave part. The dead zone model reflects the transfer torque of the master-slave part. However, the "vibro impact" model does not consider the relative displacement relationship of the master-slave part and is only applicable to the transmission of rigid objects. In this article, the dead zone model which can reflect the torque transfer between the driving part and the driven part is established [21].

The input value of the backlash part is the relative displacement $\Delta\theta$(t) between the driving part and the driven part, and the output is the output torque τ(t) of the backlash part, the dead zone model of backlash is established as follows:

$$\tau(t) = \begin{cases} k\,[\Delta\theta(t) - \alpha] + c\Delta\theta(t)', & \Delta\theta(t) > \alpha \\ 0, & |\Delta\theta(t)| \le \alpha \\ k\,[\Delta\theta(t) + \alpha] + c\Delta\theta(t)', & \Delta\theta(t) < -\alpha \end{cases} \tag{11}$$

α is 1/2 backlash width; k is stiffness coefficient of gear meshing; c is damping coefficient of gear meshing. The term $c\Delta\theta$(t)$'$ is omitted in linearization because $\Delta\theta$(t)$'$ is small. It can be seen from the above formula that the dead zone model of the backlash part is a piecewise linear function, which is linearized by the method of describing function.

Suppose that the input and output of the non-linear link can be expressed as follows:

$$x(t) = A\sin\omega t \quad y(t) = f(x) \tag{12}$$

In general, the output of sinusoidal signal is non sinusoidal periodic signal, which can be expanded into Fourier series:

$$y(t) = A_0 + \sum_{n=1}^{\infty}(A_n\cos n\omega t + B_n\sin n\omega t) \tag{13}$$

When n>1, the output response of the nonlinear link can be approximately regarded as only the fundamental component:

$$y(t) \approx A_0 + A_1\cos\omega t + B_1\sin\omega t \tag{14}$$

If and only if $A_0 = 0$, the transfer function of the nonlinear link is:

$$N(A) = \frac{L_t(A_1\cos\omega t + B_1\sin\omega t)}{L_t(A\sin\omega t)} = \frac{B_1 + jA_1}{A} \tag{15}$$

Because the dead zone model of tooth clearance is a piecewise odd function, it has the following characteristics:

$$A_1 = \frac{1}{\pi}\int_0^{2\pi}\tau(t)\cos\omega t d\omega t = \frac{1}{\pi}\int_{-\pi}^{+\pi}\tau(t)\cos\omega t d\omega t = 0 \tag{16}$$

$$A_0 = \frac{1}{2\pi}\int_0^{2\pi}\tau(t)d\omega t A_0 = \frac{1}{2\pi}\int_{-\pi}^{+\pi}\tau(t)d\omega t = 0 \tag{17}$$

$$\begin{aligned} B_1 &= \frac{1}{\pi}\int_0^{2\pi}\tau(t)\sin\omega t d\omega t \\ &= \frac{2k}{\pi}\left(\frac{A\pi}{2} - A\,arc\sin\frac{\alpha}{A} - \alpha\frac{\sqrt{A^2-\alpha^2}}{A}\right) \end{aligned} \tag{18}$$

According to the equations (15), (16), (17), (18), it can be concluded that:

$$\begin{aligned} N(A) &= \frac{B_1 + jA_1}{A} \\ &= \frac{2k}{\pi}\left(\frac{\pi}{2} - arc\sin\frac{\alpha}{A} - \frac{\alpha}{A}\sqrt{1-\frac{\alpha^2}{A^2}}\right)^{A\ge\alpha} \end{aligned} \tag{19}$$

Obviously, when the backlash width is fixed, the transfer function of the dead zone model is a variable gain link about the relative displacement of the driving part and the driven part $\Delta\theta(t)$.

The structure diagram of dead zone model of tooth clearance is shown in Fig. 5:

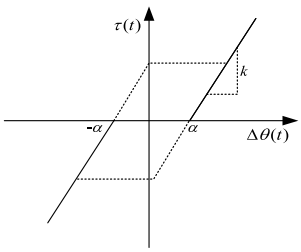

FIGURE 5. Dead zone model of gear clearance.

C. MODELING OF PERIODIC PULSATING LOAD TORQUE ON MOTOR SIDE

The load torque model of unilateral eccentric mass to motor side is shown in Fig. 6, in which: J_m is the moment of inertia, B_m is the viscosity coefficient, ω_m is the rotational speed. Where m = z,d,c, respectively represent the driving wheel, idler gear and driven wheel. N_1,N_2,N_3 are the teeth number of driving gear, idler gear and driven gear. T_{z1} is the load torque of motor drive 1# driven wheel side. T_{z2} is the load torque of motor driven idler side. T_G is the heavy torque of single eccentric wheel. T_{11} is the load torque of 1# driven wheel to driving wheel. T_{12} is the driving torque of driving wheel to 1# driven wheel. T_{21} is the load torque of driving wheel to driving wheel. T_{22} is the driving torque of driving wheel to idler. T_{23} is the load torque of 2# driven wheel to idler. T_{24} is the driving torque of the idler to 2# driven wheel.

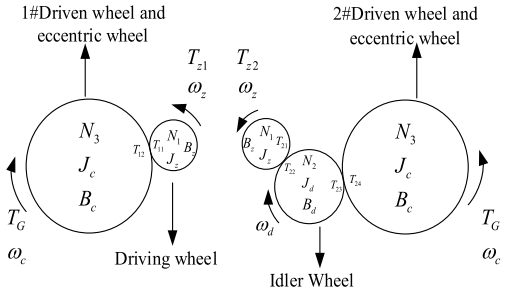

FIGURE 6. Eccentric wheel load force model.

According to the principle of torque balance, the torque balance equation from the driving wheel to the 1# driven wheel side is as follows:

$$T_{z1} = T_{11} + J_z\frac{d\omega_z}{dt} + B_z\omega_z \tag{20}$$

Similarly, for 1# driven wheel:

$$T_{12} = T_G + J_c\frac{d\omega_c}{dt} + B_c\omega_c \tag{21}$$

If the energy loss in the process of gear transmission is neglected, there exists:

$$T_{11}\omega_z = T_{12}\omega_c \tag{22}$$

Combine the meshing principle of the gear:

$$\omega_z N_1 = \omega_c N_3 \tag{23}$$

According to the equations (20), (21), (22) and (23), the following results can be obtained:

$$T_{z1} = \frac{N_1}{N_3}T_G + \left[J_z + \left(\frac{N_1}{N_3}\right)^2 J_c\right]\frac{d\omega_z}{dt} + \left[B_z + \left(\frac{N_1}{N_3}\right)^2 B_c\right]\omega_z \tag{24}$$

So far, the load model from the driving wheel to the 1# driven wheel side is established. Then the same analysis method is used to analyze the driving wheel to the idler gear and the idler to the 2# driven wheel side. After sorting out, the following formula is established:

$$T_{z2} = \frac{N_1}{N_3}T_G + \left[J_z + \left(\frac{N_1}{N_2}\right)^2 J_d + \left(\frac{N_1}{N_3}\right)^2 J_c\right]\frac{d\omega_z}{dt} + \left[B_z + \left(\frac{N_1}{N_2}\right)^2 B_d + \left(\frac{N_1}{N_3}\right)^2 B_c\right]\omega_z \tag{25}$$

The above formula is the load model from the driving wheel to the idler gear and from the idler to the 2# driven wheel side. A complete load model of eccentric wheel can be obtained by coupling equations (24) and (25):

$$T_z = \frac{2N_1}{N_3}T_G + \left[2J_z + \left(\frac{N_1}{N_2}\right)^2 J_d + 2\left(\frac{N_1}{N_3}\right)^2 J_c\right]\frac{d\omega_z}{dt} + \left[2B_z + \left(\frac{N_1}{N_2}\right)^2 B_d + 2\left(\frac{N_1}{N_3}\right)^2 B_c\right]\omega_z \tag{26}$$

In the above formula, the gravity torque of a single eccentric wheel satisfies the following requirements:

$$T_G = mgr \cdot \sin\theta_c \tag{27}$$

where m is the mass of a single eccentric, r is the distance between the center of mass and the center of rotation, θ_c is the angle of the eccentric. In order to express the eccentric load model more concisely, the equation (27) is introduced into equation (26) and the coefficients are integrated:

$$T_z = K_G \cdot \sin\theta_c + K_J\frac{d\omega_z}{dt} + K_B\omega_z \tag{28}$$

Among them, the load gravity torque coefficient $K_G = 2mgrN_1/N_3$, the load equivalent rotation inertia $K_J = 2J_z + (N_1/N_2)^2J_d + 2(N_1/N_3)^2J_c$, the equivalent viscosity coefficient $K_B = 2B_z + (N_1/N_2)^2B_d + 2(N_1/N_3)^2B_c$. When the control system is stable, the $d\omega/dt$ term is zero, so the load torque is simplified as follows:

$$T_z = K_G \cdot \sin\theta_c + K_B\omega_z \tag{29}$$

It can be seen from equation (29) that the motor side load torque consists of periodic pulsating torque and linear viscous torque. However, in the actual working condition, the amplitude of periodic pulsation is far greater than that of constant viscous torque under rated frequency condition. So the equivalent load torque can be simplified as periodic sinusoidal pulse momentum. This is equivalent to the periodic pulsating disturbance applied to the power actuator system, which increases the difficulty of controller design.

D. DYNAMIC MODELING OF ELECTRIC ACTUATOR SYSTEM

In order to analyze the stability of the electric power actuation system and design the controller parameters, it is necessary to establish the mathematical model of the controlled object. Only the driving wheel to 1# driven wheel side is selected and the rest torque is converted to one side in order to simplify the calculation and reduce the complexity of the dynamic model of electric actuator. In this way, only one gear clearance is included in the whole drive system. Then the gear clearance link is linearized with equation (19) and a complete dynamic model of electric actuator can be obtained. Combined with the torque balance equations (20), (21), (22), (23) from the driving wheel to the 1# driven wheel side, the following equations are obtained:

$$\begin{cases} T_{z1} = T_{11} + J_z \dfrac{d\omega_z}{dt} + B_z\omega_z \\ T_{12} = T_G + J_c \dfrac{d\omega_c}{dt} + B_c\omega_c \\ T_{11}N_3 = T_{12}N_1 \end{cases} \tag{30}$$

At the same time, the known armature circuit voltage equation is as follows:

$$U = RI + L\frac{di}{dt} + C_e\theta_z' \tag{31}$$

where U is the armature voltage, R is the armature circuit equivalent resistance, L is the armature circuit equivalent inductance, C_e is the back EMF coefficient, I is the armature current. Combined with equations (30), (31) and linearized expressions of gear clearance dead zone model, the complex frequency domain expression of dynamic model of electric actuator can be obtained by Laplace variation:

$$\begin{cases} U(s) = RI(s) + LsI(s) + C_e s\theta_z(s) \\ \qquad T_{z1}(s) \approx 0.5K_T I(s) \\ T_{z1}(s) = T_{11}(s) + (J_z s^2 + B_z s)\theta_z(s) \\ T_{12}(s) = T_G(s) + (J_c s^2 + B_c s)\theta_c(s) \\ \qquad T_{11}(s)N_3 = T_{12}(s)N_1 \\ T_{11}(s) = N(A)\left[\theta_z(s) - \theta_c(s)\right] \end{cases} \tag{32}$$

where: θ_z is the driving wheel angle, θ_c is the driven wheel angle, K_T is the electromagnetic torque coefficient. Equation (32) can be represented by structure diagram, as shown in Fig7.:

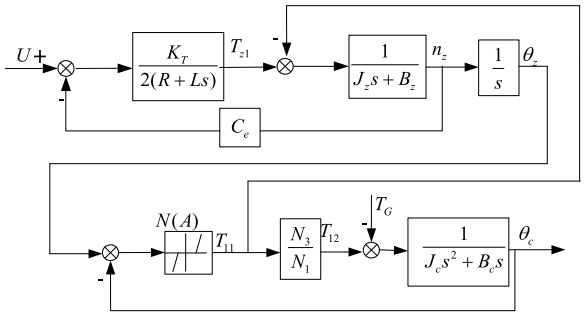

FIGURE 7. Structural block diagram of dynamic model of electric actuator.

III. ANALYSIS AND DESIGN OF POWER ACTUATOR CONTROL STRATEGY

Fig8. is the structural block diagram of the eccentric mass electric actuator system, which adopts three-loop servo control, in which APR is position loop regulator, ASR is speed loop regulator and ACR is current loop regulator. PI regulator is used for current loop and speed loop, and proportional regulator is used for position loop. The two motors in the system are independent of each other, and the control core is to realize real-time and accurate tracking of the position of the unilateral eccentric mass group, so it is necessary to design the loop parameters of the unilateral eccentric mass actuation control system.

A. STABILITY ANALYSIS AND CONTROLLER PARAMETER DESIGN OF CONTROL SYSTEM

The motor control unit is the core control unit of the actuator. Therefore, three closed-loop control models of current inner loop, speed loop and outer loop of mass block are established in this article, and then the stability of the system is analyzed, and the corresponding loop controller parameters are designed according to the stability requirements. The control loop structure of the eccentric mass actuation control system is shown in Fig. 8, where $\theta_{c1} = \omega t + \phi_1$, that is, the phase angle of the output force of one-side mass group. Similarly, the phase angle of the output force of another mass block group is $\theta_{c2} = \omega t + \phi_2$. Combined with formulas (1) and (2), it can be known that the phase tracking control of the output force on both sides can be realized by designing a reasonable controller. Combined with formula (3), it can be known that the whole electric actuator out-puts the specified composite force. The following table gives the basic technical indexes and motor parameters of electric actuator to guide the design of controller parameters.

According to the control principle of DC brush-less motor, the closed-loop control block diagram of current loop is as follows:

In order to meet the requirements of torque tracking control, PI regulator is adopted in the current loop, and zero-pole cancellation is adopted to improve the dominant pole position of the current loop. The closed-loop transfer function of the

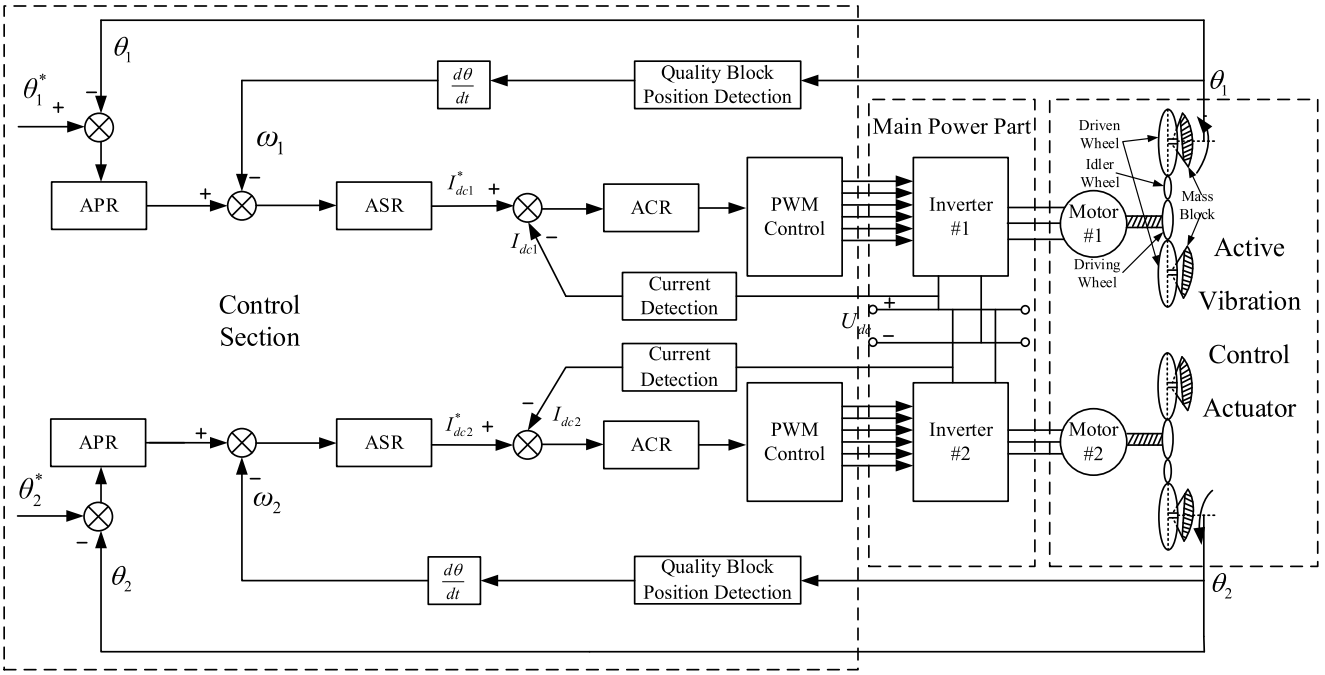

FIGURE 8. Control block diagram of active vibration control system based on servo control strategy.

TABLE 1. Basic technical indicators of electric actuators.

Technical Indicators	Value
Rated operating frequency /Hz	21.5
Accuracy of output force amplitude	≤5%
Frequency accuracy	≤0.5%
Phase steady-state accuracy	≤5%
Settling time with phase change of 30° /s	≤0.1
Settling time of force amplitude change of 300N /s	≤0.5

TABLE 2. Motor parameters.

Motor Parameters	Value
Phase resistance of stator winding R_m/Ω	0.1535
Phase inductance of stator winding L_m/mH	0.094
torque constant K_T/(mNm/A)	53.4
Speed constant K_n/(rpm/V)	179
Mechanical time constant T_m/ms	13
Equivalent moment of inertia of rotor J_m/g·cm^2	1210

current loop can be obtained as follows:

$$\Phi_i(s) = \frac{1}{2T_{\Sigma i}^2 s^2 + 2T_{\Sigma i}s + 1} \tag{33}$$

In order to meet the frequency response requirements of the speed loop, the open-loop cut-off frequency of the speed loop $\omega_{cn} < 1/(5T_{\Sigma i})$. At this time, the current loop is equivalent to the first-order inertia link, which is:

$$\Phi_i(s) = \frac{1}{2T_{\Sigma i}s + 1} \tag{34}$$

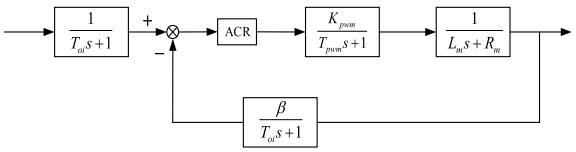

FIGURE 9. Closed-loop control block diagram of current loop.

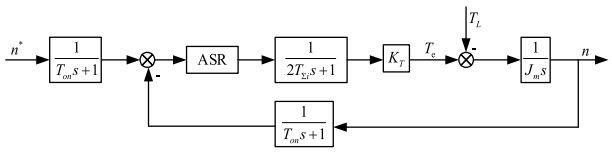

FIGURE 10. Closed-loop control block diagram of speed loop.

Fig. 10 shows a closed-loop speed control block diagram. The speed-loop parameters are designed according to the steady-state following performance.

In order to achieve no static difference in speed control, the speed loop regulator uses a PI regulator, so the speed loop is set to a typical type II system, its open-loop transfer function is:

$$G_n(s) = \frac{K_n(\tau_{ni}s + 1)}{s^2(T_{\Sigma n}s + 1)} \tag{35}$$

Among them, $K_n = K_T K_{np}/(J_m \tau_{ni})$, K_{np} is the proportional value of the speed regulator, τ_{ni} is the integral value of the speed regulator, $T_{\Sigma n} = T_{on} + 2T_{\Sigma i}$, T_{on} is the speed loop filter time constant.

In this way, the speed loop can be corrected to a typical type II third-order system, and its closed-loop transfer

function is:

$$\Phi_n(s) = \frac{K_n\tau_{ni}s + K_n}{T_{\Sigma n}s^3 + s^2 + K_n\tau_{ni}s + K_n} \tag{36}$$

According to the minimum resonance peak method in the principle of automatic control, the calculation can be obtained, $K_n = 2.449 \times 10^5$, $K_{np} = 1.94$. The step response and Bode diagram of speed loop are shown in Fig. 11:

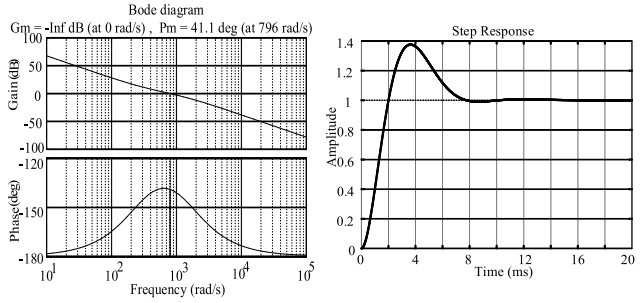

(a) Bode diagram. (b) Step response curve.

FIGURE 11. Speed loop Bode diagram and step response curve.

It can be seen from Fig. 11(a) that the phase angle margin is 41.1°, and the open-loop cut-off frequency of the speed loop is 796rad/s, which has good stability. It can be seen from Fig. 11(b) that for unit step response, the rise time is 1.37ms, the overshoot is 37.6%, and the settling time is 7.2ms, and the speed loop has excellent dynamic performance. Considering that there is a gear transmission unit between the motor side and the mass block, and because of the influence of gear lubricant, the open-loop cut-off frequency ω_{cp} of the position loop is far less than the cut-off frequency of the speed loop, therefore, the speed loop can be simplified and equivalent to a first-order inertial system, and its equivalent closed-loop transfer function is:

$$\Phi(s) = \frac{\omega_{cn}}{s + \omega_{cn}} \tag{37}$$

Among them, ω_{cn} is the open-loop cut-off frequency of the speed loop.

In order to improve the overall servo performance of the system and speed up the dynamic response to the position command, the position loop adopts a pure proportional regulator, so that the open-loop transfer function of the position loop can be obtained:

$$\Phi_p(s) = \frac{K_{pp}\omega_{cn}}{s(s + \omega_{cn})} \tag{38}$$

As shown in Fig. 12 is the position closed-loop control block diagram:

According to the characteristics of the second-order system, the damping ratio ζ_p and the natural angular frequency ω_{cn} of the position loop are:

$$\begin{cases} \xi_p \dfrac{1}{2}\sqrt{\dfrac{\omega_{cn}}{K_{pp}}} \\ \omega_{np} = \sqrt{K_{pp}\omega_{cn}} \end{cases} \tag{39}$$

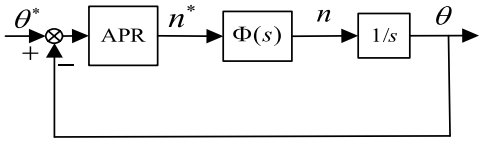

FIGURE 12. Position closed loop control block diagram.

Several groups of ζ_p values were selected for simulation experiments. According to the experimental data, $\zeta_p = 1.1$, was finally taken to calculate the proportionality factor $K_{pp} = 164.46$ of the position regulator. The position loop slope response and the Bode diagram are shown in Fig. 13.

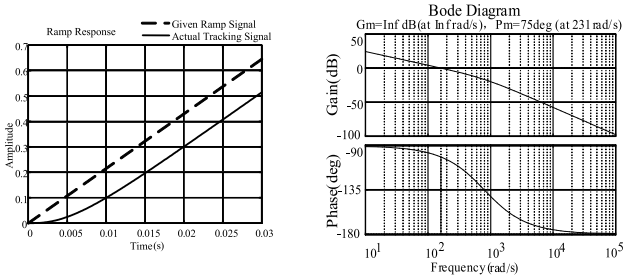

(a)Ramp response curve. (b)Bode diagram.

FIGURE 13. Ramp response curve and bode diagram of position loop.

It can be seen from fig. 13(a) that for the ramp response, the steady-state error always exists, only the tracking delay of 0.005s exists, and the dynamic performance of the position loop is good. It can be seen from fig. 13(b) that the phase angle margin is 75° and the open-loop cut-off frequency of the position loop is 231rad/s, which has good stability.

B. CONTROLLER PARAMETER CORRECTION

In order to improve the vibration mode of electric actuator, the gear clearance is usually large, which is an important nonlinear factor of the control system. In practical application, the existence of gear clearance may break the steady-state balance of the control system, and make the controller parameters fail under ideal conditions. In serious cases, it will cause the motor speed on both sides of the actuator to be out of control. Therefore, it is necessary to take the influence of gear clearance into account in the parameter design of the control system to maintain the dynamic balance of the system, so that the control system has strong adaptive ability and can meet the stability requirements of the system under different gear clearance sizes.

It can be seen from Fig.8 that the gear transmission system is included in the position ring, but outside the current ring and speed ring of the motor, the tooth clearance has a greater impact on the position ring of the system, and has less influence on the current ring and speed ring. Therefore, based on the current loop and speed loop controller parameters calculated in the previous section, the actuator position loop controller parameters are calculated iteratively to improve the robustness of the position loop, as shown in Fig. 14.

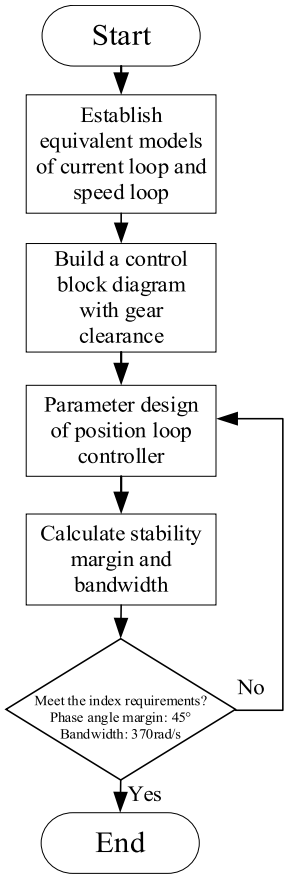

FIGURE 14. Block diagram for iterative calculation of position loop parameters.

The equivalent models of current loop and speed loop have been derived in Section III A, and the block diagram of position loop closed-loop control system with gear clearance is built by combining the equivalent control model of inner loop, as shown in Fig. 15.

In order to simplify the operation, ignoring the viscosity coefficient of the gear set, the open-loop transfer function of the position loop with gear clearance is obtained as follows:

$$G_p(s) = \frac{K_{PP}N(A)NM(s)}{N(A)NM(s)s + Js^2 + J_cM(s)s^3 + J_cJ_zs^4} \quad (40)$$

Among them, $M(\mathrm{s}) = \mathrm{ASR}K_\mathrm{T}/(2(T_{\Sigma\mathrm{n}}s+1))$, $\mathrm{N} = \mathrm{N}_3/\mathrm{N}_1$, $J = N(\mathrm{A})NJ_\mathrm{z} + N(\mathrm{A})\,J_\mathrm{c}$.

In order to analyze the influence of gear clearance on the steady-state performance of the position loop, the parameters of each regulator in the original control loop are kept unchanged.

Due to the influence of mechanical structure, the range of gear clearance size between driving and driven wheels is 0.05mm $\sim$ 0.2mm under actual working conditions. In order to explore the influence of gear clearance size on the stability of the system, the amplitude phase curve of the system is drawn when the gear clearance dimensions are 0.2mm, 0.15mm, 0.1mm, 0.05mm respectively.

It can be seen that with the increase of gear clearance size, the system cut-off frequency is higher. In the limit case, when the backlash is very large, the driving wheel and the driven wheel are out of engagement. At this time, there is no load torque hindrance for the driving wheel, and its bandwidth is naturally very high. But for the driven wheel, it loses the driving torque from the driving wheel, so the bandwidth is naturally very low. Therefore, from the perspective of the driving gear, the system bandwidth increases with the increase of the tooth clearance width, while it is opposite from the perspective of the driven wheel. Obviously, when the gear clearance size is 0.2mm, the system bandwidth is the smallest and the stability performance is the worst for the driven wheel, that is, the load.

In order to make the design parameters adapt to any possible working conditions, the limit value of gear clearance size in actual working conditions is introduced into the parameter design of the controller. According to the iterative method in Fig. 14, the controller parameters are designed to ensure the stability of the actuator control system under the worst possible working conditions, and the control system has strong self-control through high reliability of the controller parameters adaptability.

It is known that 1/2 of the maximum gear gap size between the driving wheel and the 1# driven wheel is 0.1mm. Substitute the data to obtain the position loop slope response and Bode diagram as shown in Fig. 17.

According to the analysis of the above figure, the phase angle margin is 81.8°, and the open-loop cutoff frequency of the position loop is 207rad/s. Compared with the ideal case without gear clearance, the open-loop cut-off frequency is advanced, the bandwidth is reduced, and the steady-state performance is worse; At the same time, due to the existence of gear clearance, resonance occurs at a fixed frequency point, resulting in unstable operating point. Based on the above conclusions, the parameters of the original position loop proportional regulator are no longer suitable. In the following, the parameter K_{pp} of the position loop proportional regulator is corrected according to the specific steady-state performance index.

According to the classical control theory, the steady-state performance indexes are selected as follows: the phase angle margin is 45°, and the open-loop cut-off frequency of the position loop is 370rad/s, which is more than 5 times of the rated operating frequency. Since the open-loop cut-off frequency of the position loop is advanced after the gear clearance is introduced, considering that the increase of the parameter K_{pp} of the position loop proportional regulator will increase the bandwidth and improve the response speed of the position loop, $K_{\mathrm{pp}} = 200$ is preliminarily selected. Position loop ramp response and Bode diagram are shown in Fig. 18:

It can be seen from the figure that the open-loop cut-off frequency of the position loop rises to 307rad/s, and the phase angle margin is 63°. With the increase of the parameters K_{pp} of the position loop proportional regulator, the open-loop

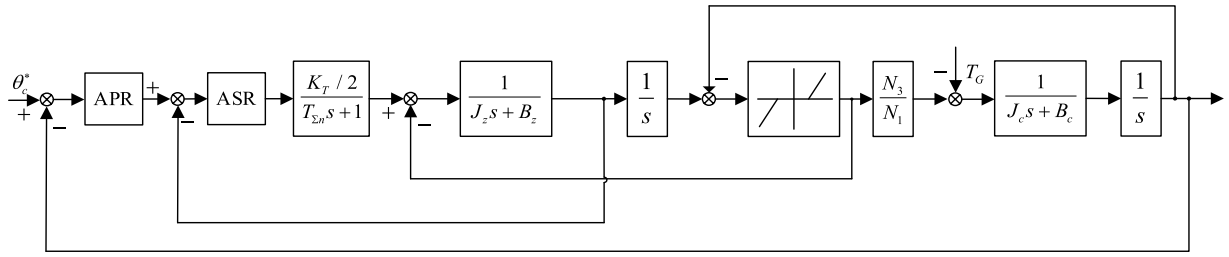

FIGURE 15. Closed-loop control diagram of position loop with gear clearance.

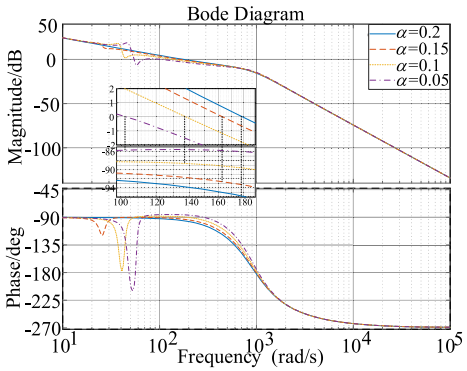

FIGURE 16. Amplitude phase curve of system under different gear clearance dimensions.

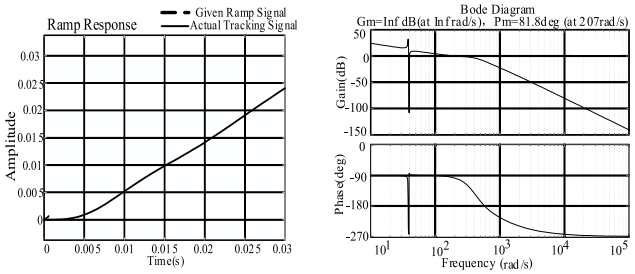

(a)Ramp response curve. (b)Bode diagram.

FIGURE 17. Position loop ramp response curve and Bode diagram with gear clearance-1.

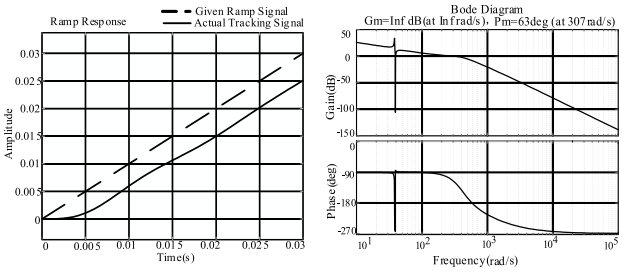

(a)Ramp response curve. (b)Bode diagram.

FIGURE 18. Position loop ramp response curve and Bode diagram with gear clearance-2.

cut-off frequency of the position loop increases and the phase angle margin decreases. According to the iterative calculation in fig. 14, $K_{pp} = 230.46$ is finally selected.

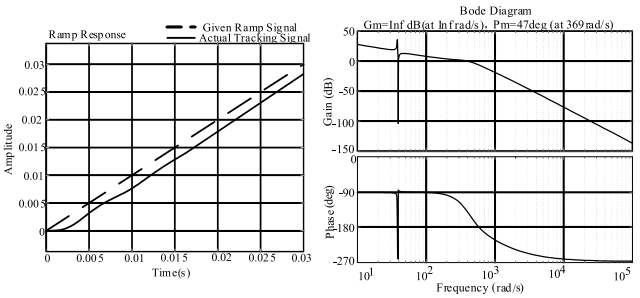

(a)Ramp response curve. (b)Bode diagram.

FIGURE 19. Position loop ramp response curve and Bode diagram with gear clearance-3.

The ramp response and Bode diagram of the position loop are shown in Fig. 19. The open-loop cut-off frequency of the position loop rises to 369rad/s, and the phase angle margin is 47°, which meets the requirements of the position loop control performance index and achieves the balance of dynamic and steady-state indexes. At the same time, comparing figs. 13 and 19, it can be seen that the tooth clearance brings resonance point to the control system, but its value is basically fixed around 18Hz, which is about 1/3 of the rated working frequency, so it basically does not affect the control of the actuator output force. In practical application, a quick start mode is generally adopted to skip the resonance point.

C. ANTI DISTURBANCE ANALYSIS OF CONTROL SYSTEM

The output force of vibration damping electric actuator is realized by the ''opposite throw'' of eccentric wheel load. The eccentric wheel load is different from other constant torque load and belongs to a kind of pulsating load, which will bring load disturbance to the control system, cause speed fluctuation and affect the performance of output force. In order to verify the reliability of the parameter correction and the disturbance rejection ability of the control system, the sensitivity H_∞ control theory should be introduced to analyze the system.

Fig. 20 shows a typical feedback control system, μ is input vector, y is output vector, e is control error vector, d is disturbance vector, $K(s)$ and $P(s)$ are transfer function matrix of controller and controlled object respectively.

Suppose $S(s)$ denotes the transfer function matrix from disturbance d to control error e, then the H_∞ norm of feedback

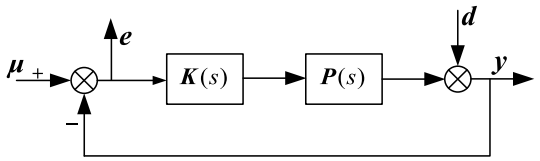

FIGURE 20. Feedback control system.

control system from disturbance to control error is defined as:

$$\|\boldsymbol{S}(s)\|_\infty = \sup_{\omega \in R^+} \bar{\sigma}\left\{\boldsymbol{S}(j\omega)\right\} \tag{41}$$

where *sup* is the supremum and $\bar{\sigma}$ is the maximum singular value of the system. It can be expressed as:

$$\bar{\sigma}\left\{\boldsymbol{S}(j\omega)\right\} = \left\{\bar{\lambda}\left[\boldsymbol{S}(j\omega)^H \boldsymbol{S}(j\omega)\right]\right\}^{1/2} \tag{42}$$

H_∞ norm is an extension of the generalized norm and a set of complex function matrices defined in H_∞ space. According to the concept of operator induced norm, the norm of closed-loop control system S(s) is defined as:

$$\|\boldsymbol{S}(s)\| = \sup_{\boldsymbol{x}\neq \boldsymbol{0}} \frac{\|\boldsymbol{S}(j\omega)\boldsymbol{x}\|_2}{\|\boldsymbol{x}\|_2} \tag{43}$$

Then, when $S(\mathrm{j}\omega) \in H_\infty$, $x \in L(-\infty, +\infty)$, we have the following conclusions:

$$\|\boldsymbol{S}(s)\| = \sup_{\boldsymbol{x}\neq \boldsymbol{0}} \frac{\|\boldsymbol{S}(j\omega)\boldsymbol{x}\|_2}{\|\boldsymbol{x}\|_2} = \sup_{\omega \in R^+} \bar{\sigma}\left\{\boldsymbol{S}(j\omega)\right\} = \|\boldsymbol{S}(s)\|_\infty \tag{44}$$

The above formula shows that the H_∞ norm of the closed-loop control system is the induced norm of the two norm of the system in H_∞ space, that is, the H_∞ norm of the transfer function matrix S(s) represents the maximum gain from disturbance to control error.

According to Fig. 20, the closed-loop transfer function from disturbance d to control error e is:

$$\boldsymbol{S}(s) = [\boldsymbol{I} + \boldsymbol{P}(s)\boldsymbol{K}(s)]^{-1} \tag{45}$$

S(s) represents the gain from the relative deviation of the open-loop characteristics to the relative deviations of the closed-loop characteristics of the control system, and is also the sensitivity function of the system [22]. By designing a reasonable controller K(s), the maximum gain of S(s), that is, the H_∞ norm of S(s), can be reduced to a small enough value, so that the relative deviation of the closed-loop system can be controlled within the allowable error range, so as to minimize the influence of disturbance on the control system.

According to Fig. 8 and combined with formulas (38) and (45), the sensitivity function of the control system can be calculated as follows:

$$\boldsymbol{S}(s) == \begin{bmatrix} \dfrac{s^2 + \omega_{cn}s}{s^2 + \omega_{cn}s + K_{\mathrm{pp}}\omega_{\mathrm{cn}}} & 0 \\ 0 & \dfrac{s^2 + \omega_{cn}s}{s^2 + \omega_{cn}s + K_{\mathrm{pp}}\omega_{\mathrm{cn}}} \end{bmatrix} \tag{46}$$

TABLE 3. H_∞ norm of control system sensitivity function under different parameters.

Kpp value	H_∞ norm
164.46	0.2501
200	0.2063
230.46	0.1611

In the simulation software, the H_∞ norm of the sensitivity function of the control system under different K_{pp} in the iteration process of section III B is calculated as follows:

It can be seen from the above table that when $K_{\mathrm{pp}} = 230.46$, the H_∞ norm of the sensitivity function of the control system is the minimum, which indicates that the energy gain from the disturbance side to the control error side is also the minimum, and the system has strong anti-interference ability and robustness.

IV. EXPERIMENTAL VERIFICATION OF ELECTRIC ACTUATING SYSTEM FOR VIBRATION SUPPRESSION

A. EXPERIMENTAL PLATFORM

By setting up the experimental platform of vibration-damping system, the performance verification experiment of electric vibration-damping actuator was carried out on the experimental platform. Hardware block diagram of power actuator for active vibration suppression is shown in Fig. 21, in which floating-point TMS320F2812 has high operation precision and fast speed, and is mainly responsible for AD sampling operation, loop PID regulator operation, magnetic codec and hall sampling operation, etc., and is also responsible for communication with the upper computer. The upper computer mainly collects some feedback data, such as load position signal, motor speed signal, bus current signal and so on. In addition, the upper computer will also participate in the loop operation of the position loop and send the speed signal command obtained after the solution to the corresponding CPU.

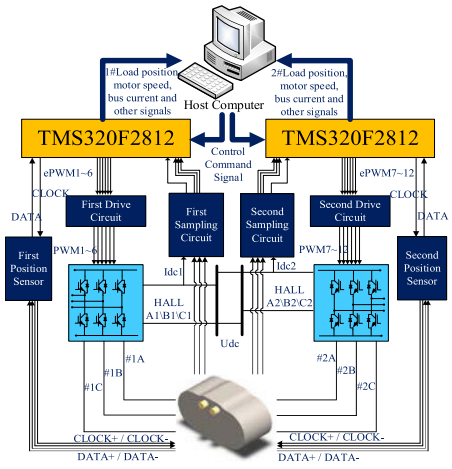

FIGURE 21. Hardware block diagram of electric actuator for active vibration suppression.

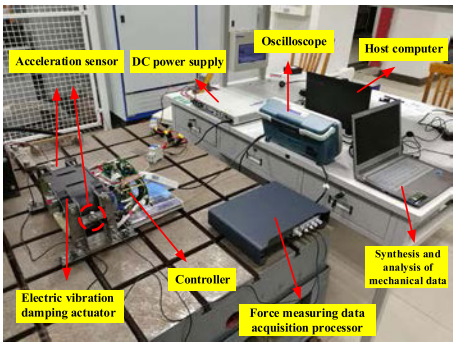

FIGURE 22. Experimental platform.

The test platform of the whole experimental system is shown in Fig. 22, which includes electric actuator and its electric drive system, DC power supply, host computer, force measuring device and other test instruments and equipment.

B. EXPERIMENTAL RESULTS

1) TEXT EXPERIMENT OF MOTOR SPEED AND PHASE CURRENT IN STEADY STATE

The control output characteristics of motor inner loop directly determine the quality of mass position loop control. The rated frequency of the actuator is 21.5Hz, which is converted to a given speed of 4000rpm on the motor side to verify the inner loop control effect of the motor.

It can be seen from Fig. 23(a) that the speed fluctuation range is 3960∼4050rpm, and the speed fluctuation amount is about 90rpm, which is less than 3% of the rated speed. At the same time, it can be seen from Fig. 23(b) that there are two states of phase current, motoring and braking, to meet the dynamic control requirements of torque. Output electric torque when rotating speed is lower than a given value, and output braking torque when rotating speed is higher than a given value.

2) TEXT EXPERIMENT OF MOTOR SPEED AND PHASE CURRENT UNDER DYNAMIC CONDITION

According to the requirement of 0.5% of the rated frequency change in the index, the test experiment of sudden drop of rated speed from 4000rpm to 300rpm is carried out, and its speed waveform and phase current waveform are shown in Fig. 24:

It only takes about 80ms to reduce the speed by 300rpm, and the overshoot is negligible, which verifies the correctness of the controller parameter design. At the same time, the phase current in Fig. 24(b) generates braking current during deceleration, which further increases the motor speed.

3) TEXT EXPERIMENT OF ACTUATOR OUTPUT FORCE ACCURACY

At this time, the positions of the masses on both sides are set to be the same, that is, the position difference is zero and the position change rate is consistent (21.5Hz). After being controlled by the mass position loop, the motor speed and current loop, the output force amplitude and frequency

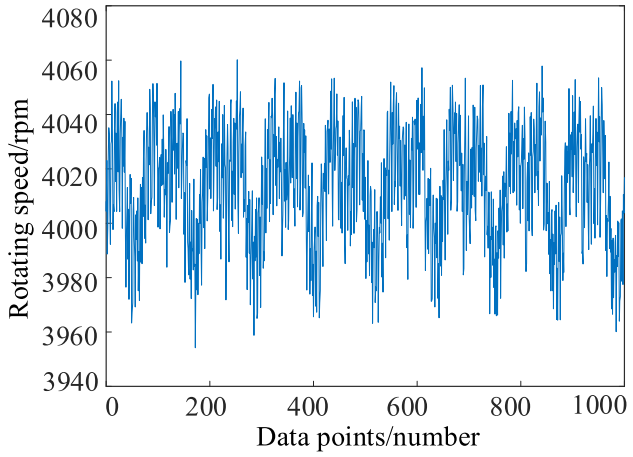

(a)Motor speed.

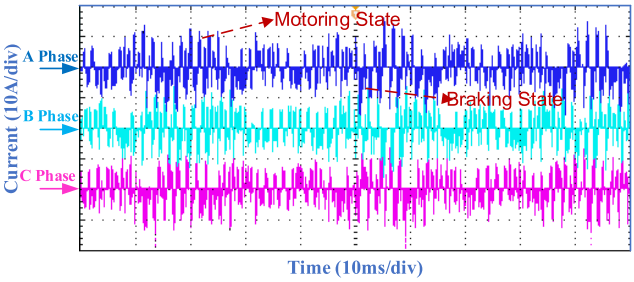

(b)Phase current.

FIGURE 23. Motor speed and phase current waveform.

waveform of the actuator system are shown in Fig. 25, and the output force amplitude reaches the theoretical maximum value of 3200±150 N, while the output frequency is 21.5Hz±0.02Hz, which meets the technical indexes of force amplitude error less than 5% and frequency difference less than 0.5%. When the position difference of the mass blocks on both sides of the design is 180°, the output force waveform of the actuator is shown in Fig. 26, and the average value of the output force is zero, and its fluctuation amplitude is less than 120N, which meets the technical requirements of no more than 150N. Therefore, it is verified that the system has high precision control ability of maximum output force and minimum output force.

In order to test the dynamic response of the output force of the actuator, by continuously changing the given position difference of the mass blocks on both sides, through the respective position tracking control, the continuous step change of the synthetic output force is realized, as shown in Fig. 27, the difference is realized. Servo tracking control of output force. Controlled at the rated frequency, the force amplitude changes every 300N from 0N to the maximum force of 2877N. The dynamic response parameters are shown in Table 4.

Due to space limitations, the figure only shows the force amplitude step response curve from 600N to 900N and 1500N to 1800N. From the table, we can see that the dynamic settling time of each force amplitude is within 0.3s, which meets

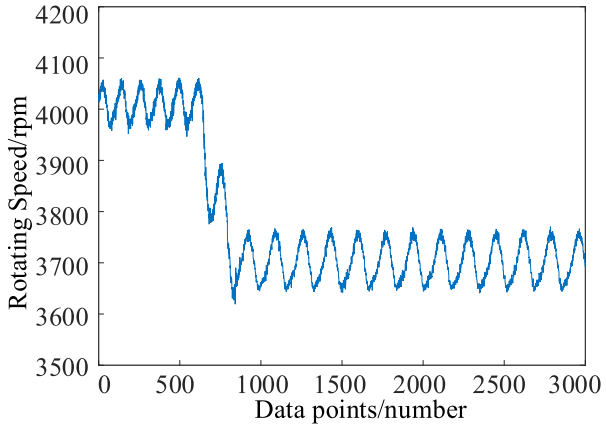

(a)Motor speed.

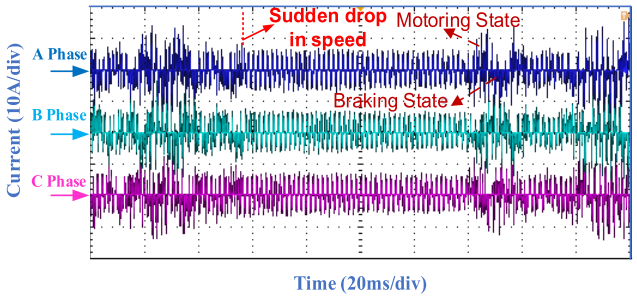

(b)Phase current.

FIGURE 24. Motor speed and phase current waveform at sudden speed drops.

TABLE 4. Experimental data of force amplitude step response.

Number	Command force (N)	Measured force amplitude (N)	Settling time t_s	Precision $\delta\%$
①	300	305-409	0.25	3.61%
②	600	580-686	0.23	3.68%
③	900	893-960	0.187	2.33%
④	1200	1179-1261	0.279	2.85%
⑤	1500	1496-1573	0.23	2.68%
⑥	1800	1778-1868	0.278	3.13%
⑦	2100	2069-2167	0.187	3.41%
⑧	2400	2351-2455	0.277	3.61%
⑨	2877	2821-2904	0.284	2.88%

the 0.5s technical index requirements. It is verified that the controller parameters balance the dynamic performance and steady-state performance of the output force well.

4) TEXT EXPERIMENT OF ACTUATOR OUTPUT FORCE PHASE CONTROL

Whether the system can effectively reduce vibration depends largely on the phase control performance of the actuator output force. Fig. 28 is the experimental results of phase mutation ±30 degrees. When the flag signal is set high, the phase mutation command is sent, and the system begins to respond to the phase change mutation command. When the output force curve coincides with the reference line of

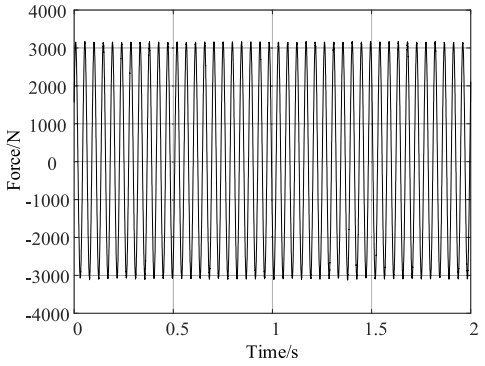

(a)Maximum force amplitude.

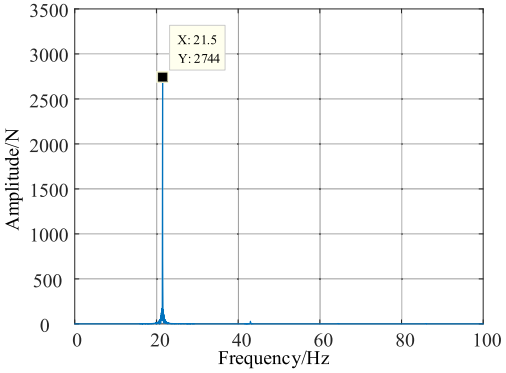

(b)Output force FFT analysis.

FIGURE 25. Frequency accuracy experiment waveform.

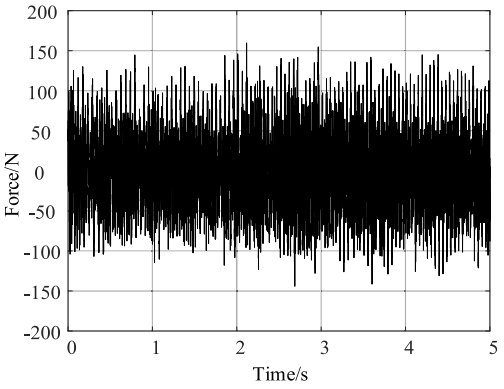

FIGURE 26. Force amplitude accuracy experiment waveform.

the given command phase, it means that the out-put force phase changes to the given command phase. It can be seen from the figure that when the phase of output force changes 30 degrees in the forward direction and 30 degrees in the reverse direction, the required settling time is 0.07s and 0.08s respectively, the dynamic settling time is less than 0.1s, and the steady-state error is less than 1 degree, which meets the technical specifications that the phase dynamic settling time is less than 0.1s and the phase steady-state accuracy is less than 5%.

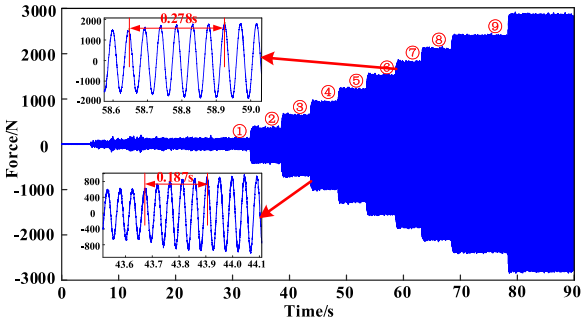

FIGURE 27. Force amplitude step response diagram.

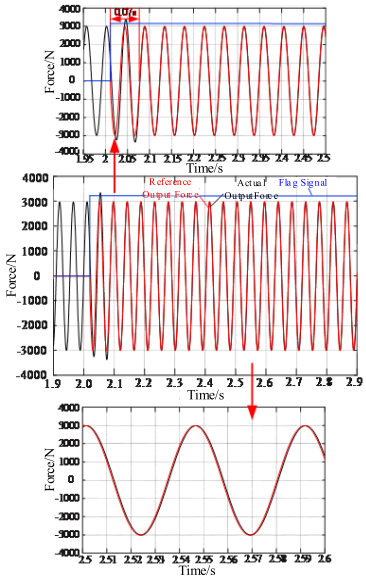

(a)Phase change 30°.

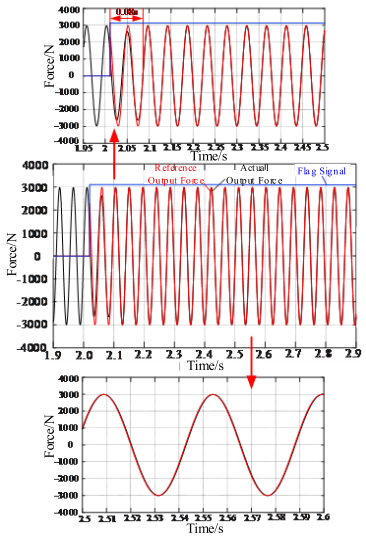

(b)Phase change -30°.

FIGURE 28. Phase change experiment waveform.

5) SYSTEM VIBRATION REDUCTION TEXT EXPERIMENT

When the vibration reduction system is not started, the original vibration level is 0.75g. As shown in Fig. 29, the system starts to reduce vibration from about 5s, and the vibration

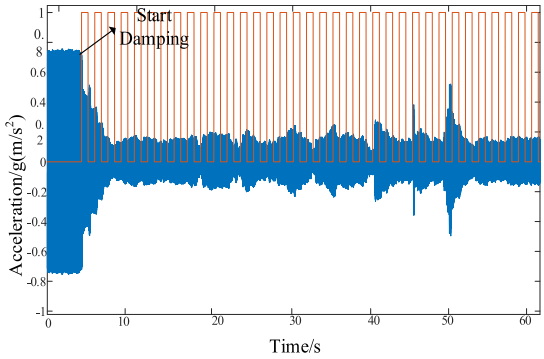

FIGURE 29. System vibration damping experiment waveform.

level in 11s drops to 0.2g and remains basically unchanged. The vibration level decays from 0.75g to 0.2g, and the damping time is less than 6s, which realizes the force amplitude, frequency and phase tracking control of the output force, achieves the system damping effect, and meets the technical index of system damping, which verifies the correctness of the system model establishment and control strategy design of the electric actuator.

V. CONCLUSION

Aiming at the vibration problem of non-fixed-wing aircraft, this article designs a control system based on an eccentric mass-type damping electric actuator. Based on theoretical deduction, a physical model of each link of the electric damping actuator is built, and the control strategy analysis model of the electric actuator control system is established. On this basis, the influence of gear clearance on the steady-state and dynamic performance of the active vibration control system is analyzed.

At the same time, combined with the three-loop servo control strategy of dual motor, the iterative calculation strategy of controller parameters considering gear clearance is proposed, and the parameters of position loop regulator are corrected by combining with stability performance index. Furthermore, the influence of gear nonlinearity on the stability and control performance of the electric actuator system is improved. At the same time, based on the sensitivity H_∞ control theory, the reliability of the controller parameter design and the robustness of the control system are verified.

An engineering prototype is developed, an experimental test platform is built. The dynamic and steady-state test experiments of the motor inner loop, the dynamic and stable test experiments of the out-put force, and the system vibration reduction level test experiments are completed. Experiments show that the actuator output force amplitude error is less than 5%, the frequency error is less than 0.5%, and the phase steady-state accuracy is less than 5%; the dynamic settling time required for a phase change of $\pm 30°$ does not exceed 0.1s, the dynamic settling time required for every 300N change in force amplitude is less than 0.3s; and the time of vibration attenuation from 0.75g to 0.2g is less than 6s.

The above experimental results meet the technical indicators. Therefore, it verifies the feasibility and correctness of the model establishment, control strategy and iterative calculation considering the gear clearance parameters, and also provides a certain theoretical design basis and technical support for the later system vibration damping experiment and prototype productization.

REFERENCES

[1] C. Trigona, B. Ando, and S. Baglio, "Measurements and investigations of helicopter-induced vibrations for kinetic energy harvesters," in *Proc. IEEE Sensors Appl. Symp. (SAS)*, Sophia Antipolis, France, Mar. 2019, pp. 1–5, doi: 10.1109/SAS.2019.8706082.

[2] V. Didkovskyi, O. Korzhyk, S. Kozeruk, A. Kozak, R. Kostiuk, and S. Liakhevych, "Noise measurement of the multicopter UAV," in *Proc. IEEE 5th Int. Conf. Actual Problems Unmanned Aerial Vehicles Develop. (APUAVD)*, Kiev, Ukraine, Oct. 2019, pp. 67–70, doi: 10.1109/APUAVD47061.2019.8943922.

[3] C. Qi-You, D. Jing-Hui, H. Jian-Ping, L. Ai-Min, and L. Ke, "Optimization selection approach for distribution of actuators in active vibration control of helicopter," in *Proc. 34th Chin. Control Conf. (CCC)*, Hangzhou, China, Jul. 2015, pp. 3248–3251, doi: 10.1109/ChiCC.2015.7260140.

[4] F. Gamar, A. K. Rusdhianto Effendie, and A. Jazidie, "Application of l1 adaptive control for helicopter vibration," in *Proc. 10th Int. Conf. Inf. Technol. Electr. Eng. (ICITEE)*, Kuta, Indonesia, Jul. 2018, pp. 1–6, doi: 10.1109/ICITEED.2018.8534897.

[5] J. Zhao, L. Liu, M. Song, and X. Zhang, "Influencing factors of anti-resonant inertial resonant machine vibration isolation system," in *Proc. 3rd Int. Conf. Comput. Comput. Sci. (COMCOMS)*, Hanoi, Vietnam, Oct. 2015, pp. 61–64, doi: 10.1109/COMCOMS.2015.22.

[6] H. Fang, Z. Zhiyi, and H. Hongxing, "Research on nonlinear co mpensation method of piezoelectric actuator in vibration control," *Vib. Shock*, vol. 29, no. 11, pp. 55–60 and 253, 2010.

[7] D.-H. Kim, T.-J. Kim, and S.-K. Paeketal, "Application and performance evaluation of helicopter active vibration control system for surion," *J. Korean Soc. Aeronaut. Space Sci.*, vol. 43, no. 6, pp. 557–567, 2015.

[8] R. Blackwell and T. Millott, "Dynamic design characteristic of the Sikorsky X2 technology TM demonstrator aircraft," in *Proc. 46th Annu. Forum Amer. Helicopter Soc.*, Montreal, QC, Canada, 2008.

[9] Y. Sun, "Design and experimental studies of an active vibration absorber with adjustable time delay," in *Proc. Int. Conf. Adv. Mech. Syst. (ICAMechS)*, Xiamen, China, Dec. 2017, pp. 386–391, doi: 10.1109/ICAMechS.2017.8316504.

[10] Y. Gao and L. Li, "Model of the active vibration isolation platform with magnetostrictive actuators," in *Proc. IEEE Int. Conf. Autom. Logistics*, Qingdao, China, Sep. 2008, pp. 346–350, doi: 10.1109/ICAL.2008.4636173.

[11] Y. Feiyi, "Design and application of a new active vibration absorber," Harbin Eng. Univ., Harbin, China, Tech. Rep., 2015.

[12] Z. Yan, L. Aimin, and C. Quanlong, "Vibration response prediction and vibration reduction analysis of airframe," *Helicopter Technol.*, no. 1, pp. 13–18, 2015

[13] Y. Tiejun, J. Guoyong, L. Xiaoyou, L. Zhigang, Z. Wenping, and W. Zhiqiu, "Research on active vibration control technology of ship power plant," *Ship Sci. Technol.*, no. 2, pp. 46–53, 2006.

[14] Z. Shi and Z. Zuo, "Backstepping control for gear transmission servo systems with backlash nonlinearity," *IEEE Trans. Autom. Sci. Eng.*, vol. 12, no. 2, pp. 752–757, Apr. 2015, doi: 10.1109/TASE.2014.2369430.

[15] W. Kim, D. Shin, D. Won, and C. C. Chung, "Disturbance-observer-based position tracking controller in the presence of biased sinusoidal disturbance for electrohydraulic actuators," *IEEE Trans. Control Syst. Technol.*, vol. 21, no. 6, pp. 2290–2298, Nov. 2013, doi: 10.1109/TCST.2013.2237909.

[16] W. Zhaogang, "Iterative calculation method for launching position and velocity error of inertial navigation measurement," *Acta Ballistics*, vol. 27, no. 2, pp. 29–33, 2015.

[17] Y. Wu, N. Sun, H. Chen, and Y. Fang, "Adaptive output feedback control for 5-DOF Varying-Cable-Length tower cranes with cargo mass estimation," *IEEE Trans. Ind. Informat.*, early access, Jun. 30, 2020, doi: 10.1109/TII.2020.3006179.

[18] S. Ji and A. Wu, "Study on dual-loop controller of helicopter based on the robust H-infinite loop shaping and mixed sensitivity," in *Proc. Int. Conf. Electr. Control Eng.*, Yichang, China, Sep. 2011, pp. 1291–1294, doi: 10.1109/ICECENG.2011.6057783.

[19] Z. Ming, "Study on active vibration isolation method based on robust control theory," Harbin Inst. Technol., Harbin, China, Tech. Rep., 2019.

[20] P. Vartholomeos, K. Vlachos, and E. Papadopoulos, "Analysis and motion control of a centrifugal-force microrobotic platform," *IEEE Trans. Automat. Sci. Eng.*, vol. 10, no. 3, pp. 545–553, Jul. 2013.

[21] G. Lai, G. Tao, and Y. Zhang, "Adaptive control of noncanonical nonlinear systems with unknown input dead-zone characteristics," in *Proc. IEEE Conf. Decis. Control (CDC)*, Miami Beach, FL, USA, Dec. 2018, pp. 5524–5529, doi: 10.1109/CDC.2018.8618896.

[22] Y. Zhang, J. Wu, and Y. Xu, "The application of H_∞/mixed sensitivity approach to attitude control system for a winged missile," in *Proc. 5th World Congr. Intell. Control Autom.*, Hangzhou, China, Dec. 2004, pp. 748–751, doi: 10.1109/WCICA.2004.1340685.

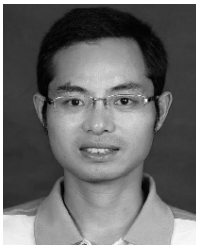

ZHENYANG HAO (Member, IEEE) received the bachelor's degree in electrical engineering from Nanjing Normal University in 2004 and the master's and Ph.D. degrees in power electronics and motion drive from the Nanjing University of Aeronautics and Astronautics in 2010.

He has been an Associate Professor with the Department of Electrical Engineering, Nanjing University of Aeronautics and Astronautics, since 2013. His research interests include new energy power electronic conversion technology, aviation power supply and power actuator technology, electric vehicle motor design, and driving technology.

TAO WANG received the degree in electrical engineering and automation from Anhui University in 2019. He is currently pursuing the master's degree in electrical engineering with the Nanjing University of Aeronautics and Astronautics, China. His main research direction includes active vibration control and motor control.

XIN CAO (Member, IEEE) received the B.Eng., M.Sc., and Ph.D. degrees in electrical engineering from the Nanjing University of Aeronautics and Astronautics, Nanjing, China, in 2003, 2006, and 2010, respectively, all in electrical engineering.

Since 2011, he has been with the Nanjing University of Aeronautics and Astronautics. From 2011 to 2012, he was a Research Associate with the Department of Aeronautical and Automotive Engineering, Loughborough University, Loughborough, U.K. His current research interests include distributed generation and renewable energy, electric vehicles, switched reluctance motors, and magnetically levitated bearingless motors.

QIYAO ZHANG (Student Member, IEEE) received the degree in electrical engineering and automation from the Nanjing University of Aeronautics and Astronautics, China, in 2020, where she is currently pursuing the master's degree in electrical engineering. Her main research direction is motor control.